




Electrostatic turbulence in EAST plasmas with internal transport barrier

Yuehao Ma¹, Bin Zhang² , Jian Bao^{3,*}, Z. Lin⁴, Wenlu Zhang³ , Huishan Cai^{1,*} 
and Ding Li^{3,5,6}

¹ CAS Key Laboratory of Geospace Environment, School of Nuclear Sciences and Technology, University of Science and Technology of China, Hefei 230026, China

² Institute of Plasma Physics, Chinese Academy of Sciences, Hefei 230031, China

³ Institute of Physics, Chinese Academy of Sciences, Beijing 100190, China

⁴ Department of Physics and Astronomy, University of California, Irvine, CA 92697, United States of America

⁵ Songshan Lake Materials Laboratory, Dongguan, Guangdong 523808, China

⁶ University of Chinese Academy of Sciences, Beijing 100049, China

E-mail: jbao@iphy.ac.cn and hscai@mail.ustc.edu.cn

Received 20 December 2022, revised 19 February 2023

Accepted for publication 3 March 2023

Published 30 March 2023



CrossMark

Abstract

Based on first-principles nonlinear gyrokinetic simulations, the electrostatic turbulence properties in the internal transport barrier (ITB) region of an Experimental Advanced Superconducting Tokamak discharge (#93890) are investigated. Specifically, ITBs with steep density and temperature gradients are located in the weakly negative magnetic shear region at the plasma center. In the linear stage, the growth rate and frequency of the ion temperature gradient (ITG) mode increase significantly due to resonant excitation by trapped electrons. That is, the resonance between trapped electrons and the ITG becomes strong due to the precession drift reversal of trapped electrons by the negative magnetic shear and Shafranov shift. Meanwhile, the trapped electron mode is stable in the ITB region due to only a very small fraction of electrons precessing in the direction of the electron diamagnetic drift. Nonlinear simulations show that, after considering the non-adiabatic effect of trapped electrons, the heat conductivity of ions and the turbulence intensity increase by at least a factor of 7 compared with the results only considering the adiabatic effect of electrons. The zonal charge density of trapped electrons can partially cancel that of ions, which weakens the intensity of the zonal flow, and consequently reduces the zonal flow regulation and enhances the turbulent transport.

Keywords: trapped electrons, ion temperature gradient, internal transport barrier, zonal flow, EAST

(Some figures may appear in colour only in the online journal)

* Authors to whom any correspondence should be addressed.



Original Content from this work may be used under the terms of the [Creative Commons Attribution 4.0 licence](https://creativecommons.org/licenses/by/4.0/). Any further distribution of this work must maintain attribution to the author(s) and the title of the work, journal citation and DOI.

1. Introduction

Turbulent transport is the dominant mechanism that degrades the plasma confinement in tokamaks [1]. Thus, it is of great significance to understand the properties of the corresponding microscopic drift wave instability and turbulence. The confinement performance of the tokamak has been significantly improved by forming internal transport barriers (ITBs) in the core region [2–6]. Inside the ITBs, the gradient of the temperature and density is high due to the reduction of anomalous transport caused by turbulence such as the ion temperature gradient (ITG) mode and trapped electron mode (TEM). Therefore, the turbulent transport is closely related to the formation of ITBs.

The turbulent transport is affected not only by the $\mathbf{E} \times \mathbf{B}$ shear flow and geometry effects of plasma (such as magnetic shear, Shafranov shift) [3, 4, 7–17], but also by the effects of trapped electrons [3, 18–25]. It has been theoretically demonstrated that turbulence can nonlinearly generate zonal flow through modulational instability based on first-principle gyrokinetics [10], which in turn effectively regulate turbulence and reduce the transport level from Bohm type to gyro-Bohm type as the tokamak size increases [12]. Furthermore, by applying the cyclone base case (CBC) parameters [26] with a monotonic q profile with positive magnetic shear, it was found that the growth rate of ITG mode is enhanced by the non-adiabatic effect of trapped electrons [19, 20]. Correspondingly, the heat conductivity of ions also increases compared with that obtained from simulations only including the adiabatic effect of electrons [18–20]. It was shown that the trapped electrons can enhance the ITG growth rate by decreasing the adiabatic electron shielding effect, and most trapped electrons do not respond to the ITG mode in the positive magnetic shear [21]. Moreover, the effects of trapped electrons only slightly increase the excitation threshold of ITG instability in reversed field pinch plasmas based on the eigenvalue approach [24, 25].

However, so far, the effects of trapped electrons on turbulence in ITB plasmas with negative magnetic shear have been poorly studied. Nonlinear gyrokinetic studies on ITB plasma turbulent transport using realistic experimental parameters, in which the mechanism can be complicated by the Shafranov shift and wave–particle interactions, are desirable. In this work, based on the realistic equilibrium of the Experimental Advanced Superconducting Tokamak (EAST) discharge (#93890) [6], where a core ITB forms in the presence of weakly negative magnetic shear, we carry out linear and nonlinear simulations of electrostatic drift wave instability and turbulence by using the first-principles gyrokinetic toroidal code (GTC) [27].

This paper is organized as follows: the physics model and simulation parameters are introduced in section 2, the linear properties of drift wave instability in the ITB region, including dispersion relation, mode structure and phase space resonance are studied in section 3, and the effects of trapped electrons on zonal flow generation, turbulence nonlinear saturation and transport mechanisms are investigated and elucidated in section 4. Finally, a summary and discussions are given in section 5.

2. Physics model and simulation parameters

2.1. Physics model

The nonlinear gyrokinetic model is used to study the electrostatic turbulence in the ITB plasmas in this work. The gyro-center dynamics are described by the gyrokinetic Vlasov equation in five-dimensional phase space, using the gyro-center position \mathbf{X} , magnetic moment μ , and parallel velocity v_{\parallel} as independent variables: [28, 29]

$$\frac{d}{dt} f_{\alpha}(\mathbf{X}, \mu, v_{\parallel}, t) \equiv \left[\frac{\partial}{\partial t} + \dot{\mathbf{X}} \cdot \nabla + v_{\parallel} \frac{\partial}{\partial v_{\parallel}} - \mathcal{C}_{\alpha} \right] f_{\alpha} = 0, \quad (1)$$

$$\dot{\mathbf{X}} = v_{\parallel} \frac{\mathbf{B}_0}{B_0} + \mathbf{v}_E + \mathbf{v}_c + \mathbf{v}_g \quad (2)$$

$$\dot{v}_{\parallel} = -\frac{1}{m_{\alpha}} \frac{\mathbf{B}^*}{B_0} \cdot (\mu \nabla B_0 + Z_{\alpha} \nabla \bar{\phi}) \quad (3)$$

$$\mathbf{B}^* = \mathbf{B}_0 + \frac{B_0 v_{\parallel}}{\Omega_{\alpha}} \nabla \times \mathbf{b}_0 \quad (4)$$

where f_{α} is the particle distribution function. The collision operator \mathcal{C}_{α} in GTC [30, 31] is not turned on in this work due to the high temperature in ITB plasmas. The subscript $\alpha = i, e$ represents the ion and electron species. Z_{α} , m_{α} and Ω_{α} are the particle charge, mass and the cyclotron frequency, respectively. $\mathbf{B}_0 = B_0 \mathbf{b}_0$ is the equilibrium magnetic field. The overbar stands for the gyrophase average; for example, $\bar{\phi} = \frac{1}{2\pi} \int \phi \delta(\mathbf{X} + \boldsymbol{\rho}_{\alpha} - \mathbf{x}) d\mathbf{x} d\theta$ is the gyrophase-averaged electrostatic potential, \mathbf{x} is the particle position, θ is the gyrophase angle, and $\boldsymbol{\rho}_{\alpha}$ is the gyroradius. The $\mathbf{E} \times \mathbf{B}$ drift velocity $\mathbf{v}_E = c \mathbf{b}_0 \times \nabla \bar{\phi} / B_0$, the curvature drift velocity $\mathbf{v}_c = v_{\parallel}^2 \nabla \times \mathbf{b}_0 / \Omega_{\alpha}$, and the grad-B drift velocity is $\mu / (m_{\alpha} \Omega_{\alpha}) \mathbf{b}_0 \times \nabla B_0$. The gyrokinetic Poisson's equation is

$$\frac{4\pi Z_i^2 n_i}{T_i} (\phi - \bar{\phi}) = 4\pi (Z_i \bar{n}_i - e n_e) \quad (5)$$

where $\bar{\phi}(\mathbf{x}, t) = \frac{1}{n_i} \int d\mathbf{v} \bar{\phi}(\mathbf{X}, t) f_{i0}(\mathbf{X}, v_{\parallel}, \mu, t)$ is the second gyrophase-averaged potential, and f_{i0} is the ion equilibrium distribution. $\bar{n}_i = \int d\mathbf{v} f_i(\mathbf{X}, v_{\parallel}, \mu, t)$ and $n_e = \int d\mathbf{v} f_e(\mathbf{x}, v_{\parallel}, \mu, t)$ are the gyrophase-averaged ion and electron densities, respectively (note that the reduction of equation (1) in the drift kinetic limit is applied for electron species due to its small gyroradius), where $\int d\mathbf{v} = \frac{2\pi}{m_i} \int B_{\parallel} dv_{\parallel} d\mu \frac{1}{2\pi} \int \delta(\mathbf{X} + \boldsymbol{\rho}_{\alpha} - \mathbf{x}) d\mathbf{X} d\theta$, and $B_{\parallel}^* = \mathbf{b}_0 \cdot \mathbf{B}^*$. It should be noted that we split the electrostatic potential and gyro-center density into zonal and non-zonal parts as $\phi = \langle \phi \rangle + \delta\phi$, $n = \langle n \rangle + \delta n$, where the zonal part is calculated using the flux-surface average operation $\langle \phi \rangle \equiv \oint d\theta d\zeta J \phi / (\oint d\theta d\zeta J)$ (J is the Jacobian of the Boozer coordinates, θ is the poloidal angle, and ζ is the toroidal angle), and the non-zonal parts satisfy $\langle \delta\phi \rangle = \langle \delta n \rangle = 0$. Meanwhile, the electron response is adiabatic only for the non-zonal component [32]. In order to achieve better numerical accuracy, we solve the gyrokinetic Poisson's equation for zonal and non-zonal fields separately, and the zonal field equation is [33]

$$\langle \nabla_{\perp}^2 \phi \rangle = \left\langle \left(\frac{T_i}{\rho_i^2 n_i Z_i^2} - \frac{T_i}{n_i Z_i^2} \nabla_{\perp}^2 \right) (en_e - Z_i \bar{n}_i) \right\rangle \quad (6)$$

where the Padé approximation is used to numerically solve the above equation by retaining the finite Larmor radius effect on the ion polarization density. The non-zonal field equation can be described by equation (5) by introducing Padé approximation as well.

In principle, equations (1)–(3) and (5) can form a closed system for the electrostatic full-f simulation. However, the full-f simulation incorporating ion and electron dynamics simultaneously is challengeable due to the realistic electron–ion mass ratio and high particle noise of full distribution. Thus, we apply the δf method [34, 35] for ion species and the fluid–kinetic hybrid model [21, 36] for electron species in order to improve the numerical accuracy and efficiency. In order to decrease particle noises, a perturbative δf method has been developed which splits the total distribution function into the equilibrium and perturbed parts ($f_{\alpha} = f_{\alpha 0} + \delta f_{\alpha}$, with $\delta f_{\alpha} \ll f_{\alpha 0}$), where the equilibrium part $f_{\alpha 0}$ remains unchanged, and only the perturbed part δf_{α} is evolved in the simulation. The equilibrium distribution satisfies the following equation:

$$\frac{\partial f_{\alpha 0}}{\partial t} + (\mathbf{v}_{\parallel} \mathbf{b}_0 + \mathbf{v}_c + \mathbf{v}_g) \cdot \nabla f_{\alpha 0} - \frac{\mu}{m_{\alpha}} \frac{\mathbf{B}^*}{B_0} \cdot \nabla B_0 \frac{\partial f_{\alpha 0}}{\partial v_{\parallel}} = 0 \quad (7)$$

where f_0 can be approximated as a Maxwellian distribution when the neoclassical effect is not included. Defining the particle weight $w_{\alpha} = \delta f_{\alpha} / f_{\alpha}$, we can then obtain the particle weight equation from equations (1) and (7).

$$\frac{dw_{\alpha}}{dt} = (1 - w_{\alpha}) \left(-\mathbf{v}_E \cdot \frac{\nabla f_{\alpha 0}}{f_{\alpha 0}} + Z_{\alpha} \frac{\mathbf{B}^*}{B_0} \cdot \nabla \phi \frac{1}{m_{\alpha} f_{\alpha 0}} \frac{\partial f_{\alpha 0}}{\partial v_{\parallel}} \right) \quad (8)$$

which is solved for δf_i in the simulation. However, the temporal and spatial scales are disparate between ions and electrons when using the realistic electron–ion mass ratio, and it is no longer efficient to apply the δf method to electron dynamics. In order to improve the numerical properties for kinetic electron simulation of ion-scale turbulence, a fluid–kinetic electron hybrid model is developed [36] by further splitting the perturbed distribution into adiabatic and non-adiabatic responses as

$$\delta f_e = \frac{e \delta \phi}{T_e} f_{e0} + \delta g_e \quad (9)$$

Both $\delta \phi$ and δg_e are solved iteratively based on the assumption that the adiabatic response is larger than the non-adiabatic response [21]. By expanding $\delta \phi$ using a small parameter $\delta = \omega / (k_{\parallel} v_{the})$: $\delta \phi = \delta \phi^{(0)} + \delta \phi^{(1)} + \dots$, the Poisson equation (5) becomes

$$\frac{4\pi Z_i^2 n_{i0}}{T_i} \left(\delta \phi^{(0)} - \delta \tilde{\phi}^{(0)} \right) + \frac{4\pi e^2 n_{e0}}{T_e} \delta \phi^{(0)} = 4\pi Z_i^2 \delta \bar{n}_i \quad (10)$$

where $\delta \bar{n}_i = \int \delta f_i d\mathbf{v}$. Then δg_e is solved by using particle-in-cell simulation in the higher order, of which the dynamic equation is given by

$$\frac{d}{dt} \delta g_e^{(1)} = -\mathbf{v}_E \cdot \nabla f_{e0} + f_{e0} (\mathbf{v}_c + \mathbf{v}_g) \cdot \nabla \left(\frac{e \langle \phi \rangle}{T_e} \right) - \mathbf{v}_E \cdot \nabla \delta f_e^{(0)} - \frac{\partial \delta f_e^{(0)}}{\partial t} \quad (11)$$

where $\delta f_e^{(0)} = e f_{e0} \delta \phi^{(0)} / T_e$. Substituting the non-adiabatic electron density $\delta n_e^{(1)} = \int \delta g_e^{(1)} d\mathbf{v}$ into equation (5) while considering equation (9), we derive the Poisson equation with the first-order correction on $\delta \phi$ as

$$\frac{4\pi Z_i^2 n_{i0}}{T_i} \left(\delta \phi^{(0+1)} - \delta \tilde{\phi}^{(0+1)} \right) + \frac{4\pi e^2 n_{e0}}{T_e} \delta \phi^{(0+1)} = 4\pi \left(Z_i \delta \bar{n}_i - e \delta n_{e(\text{loop}=1)} \right) \quad (12)$$

where $\delta \phi^{(0+1)} = \delta \phi^{(0)} + \delta \phi^{(1)}$. Following the above equations, more iteration loops can be repeated until the results converge. Please note that the valid condition for the fluid–kinetic electron model requires the adiabatic part to be dominant, otherwise the result diverges with the loop time. In short, the fluid–kinetic electron model in GTC has a hierarchy of physics levels that treat electrons as adiabatic fluid in the lowest order, and incorporates the non-adiabatic kinetic effects in the higher order.

2.2. Simulation setup

In this work, we present linear and nonlinear simulations of electrostatic turbulence based on EAST tokamak discharge #93890 at 5000 ms [6]. The EAST discharge #93890 is diagnosed with the plasma profiles and magnetic geometry as reported in [6], where both the electron and ion density and the temperature exhibit ITBs in the presence of weakly negative magnetic shear. The detailed parameters are given as follows. The on-axis major radius is $R_0 = 1.91$ m, the minor radius at the wall of the outer mid-plane is $a = 0.41$ m, and the on-axis magnetic field is $B_a = 1.49$ T. From figure 1, it is seen that both the density and temperature ITBs are located at around $0.2 < r/a < 0.3$, where the ion and electron temperature profiles are similar, and R_0/L_T peaks at 18. Meanwhile, the maximum value of η_i is located at $r/a = 0.25$, which provides the toroidal ITG drive. Thus, the simulation domain for ITB turbulent transport is set between $r/a = 0.1$ and $r/a = 0.5$ with the Dirichlet boundary condition, which is based on the consideration that turbulence perturbations are negligibly small near the inner and outer simulation boundaries. In the ITB region, the q profile is relatively flat around $q \approx 1$ (at $r/a = 0.25$, $q = 1$, $s = rdq/(qdr) = -0.13$). In this work, for the global gyrokinetic simulation of turbulent transport in ITB plasmas, three key equilibrium features are considered, including the weakly negative magnetic shear, the steep gradients of both the temperature and density profiles, and the Shafranov shift effect [17, 22].

The important simulation parameters used for physics runs with convergence are listed as follows. For the simulations of the core, 150 radial grids, 32 parallel grids and 25 grids per poloidal wavelength are sufficient. The time step is $\Delta t =$

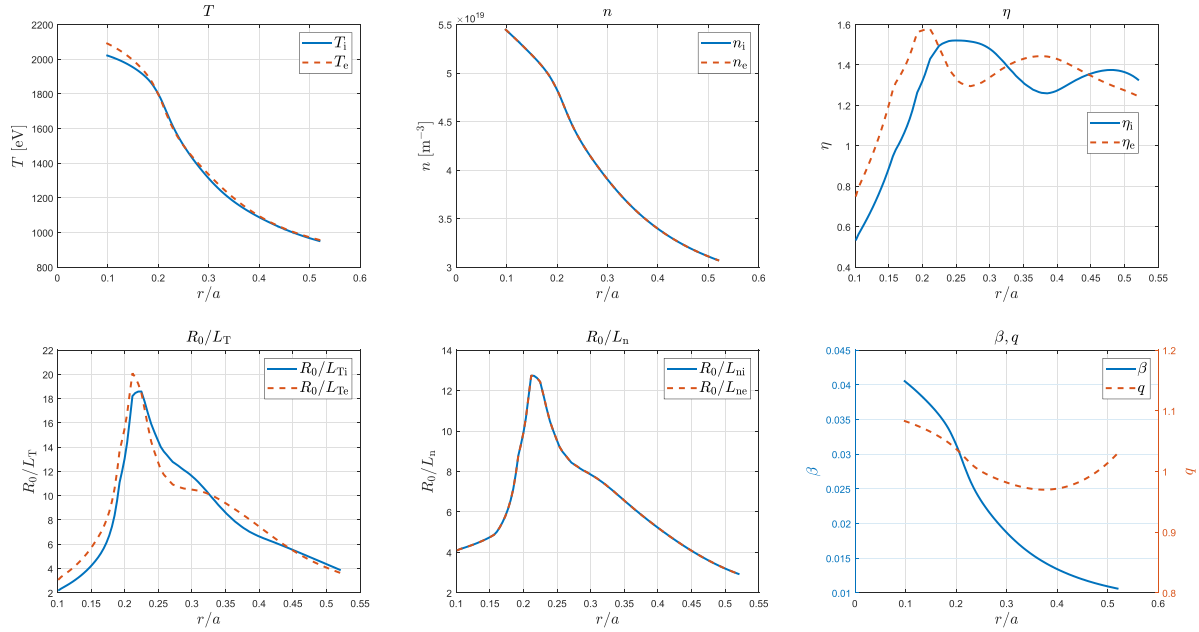


Figure 1. Plasma radial profiles in EAST discharge #93890 at 5000 ms in the range of $r/a \in [0.1, 0.5]$. The top row, from left to right, shows temperatures (T), density (n) and $\eta = L_n/L_T$ for ions (subscript i) and electrons (subscript e), respectively. The bottom row, from left to right, shows the inverse temperature length scales (R_0/L_T), the inverse density length scale (R_0/L_n), the safety factor (q) and the ratio of the plasma pressure to the magnetic pressure ($\beta = 8\pi P_0/B_0^2$).

$0.005R_0/C_s$, where C_s is the on-axis ion sound speed. For better numerical properties, the maker density and temperature profiles are uniformly loaded, using the values at the maximum η_i location in figure 1 ($r/a = 0.25$). Meanwhile, the more important plasma gradients are still accurately calculated from each profile in figure 1, which can provide a realistic drive for the instability.

3. Linear simulation results

The GTC nonlinear electrostatic gyrokinetic model introduced in section 2 has been well verified and validated for turbulence simulations [21, 27]. In this paper, the adiabatic electron model means that only the adiabatic effect of electrons is included. For the non-adiabatic electron model, besides the adiabatic effect of electrons, the non-adiabatic effect of trapped electrons is included, while the non-adiabatic effect of the passing electrons is not considered, because the non-adiabatic response is dominated by trapped electrons in the low-frequency regime of microturbulence [19, 21]. In this section, we carry out GTC simulations to study the linear properties of electrostatic drift wave instability in EAST ITB plasmas.

3.1. Growth rate of ITG mode is drastically enhanced by trapped electrons

In order to obtain the linear spectra within the radial simulation domain in figure 1, we first perform the toroidal mode number n (or $k_\theta \rho_i = (nq/r)\rho_i$) scan by using the adiabatic electron model in which the electron response is adiabatic. The

dependencies of mode real frequency and growth rate versus $k_\theta \rho_i$ are shown by the blue lines in figure 2, which is identified as an ITG mode because the mode frequency is in the direction of the ion diamagnetic drift, and only the ITG destabilization mechanism is included in the adiabatic electron model.

In the non-adiabatic electron simulation, the real frequency and growth rate are shown by the red line in figure 2. It can be seen that the frequency is still in the direction of the ion diamagnetic drift and significantly increases with the non-adiabatic effect of trapped electrons. This is different from the result shown in [21], where it was shown that the frequency of ITG is not sensitive to the electron response. The growth rate of the ITG mode is dramatically enhanced (by at least 100%) in the non-adiabatic electron model, especially for shorter wavelengths, by a factor of 3–4. The peak value ($k_\theta \rho_i \approx 1$) in the ITG spectra is also larger than that in the conventional ITG, such as in the CBC case [19, 21, 26]. It can also be found that the growth rate and frequency have very little variation after $k_\theta \rho_i > 1.5$, where the stabilization effect of the finite Larmor radius is large.

In order to identify the mode and elucidate the physics mechanism, figure 3 illustrates the electrostatic potential mode structure of the most unstable case at the peak location ($n = 25, m = 25$) of the $k_\theta \rho_i$ spectra, which does not change much compared with that in the adiabatic electron case. The intensity of mode amplitude peaks at the largest η_i location. Thus, it is confirmed that the ITG mode is the dominant electrostatic drift wave instability in EAST ITB plasmas, rather than the TEM. The 2D mode structure of ITG exhibits a balloon-like structure that peaks around the outer midplane as shown in figures 3(b) and (d). However, the radial profiles of neighboring poloidal harmonics (i.e. m and $m \pm 1$) almost overlap with each other

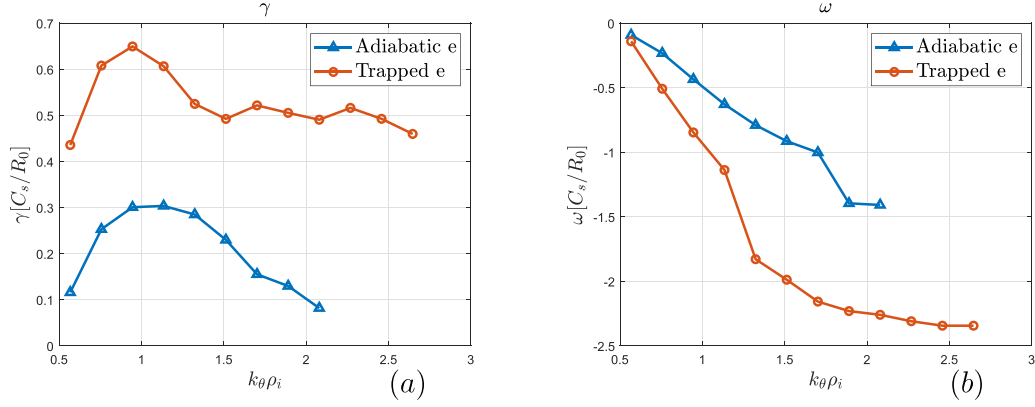


Figure 2. For kinetic electron (circle lines) and adiabatic electron (triangle lines) simulations, dependence of growth rate (a) and real frequency (b) on poloidal wavelength $k_\theta \rho_i$ (corresponding to toroidal mode number $n = 15, 20, \dots, 50$).

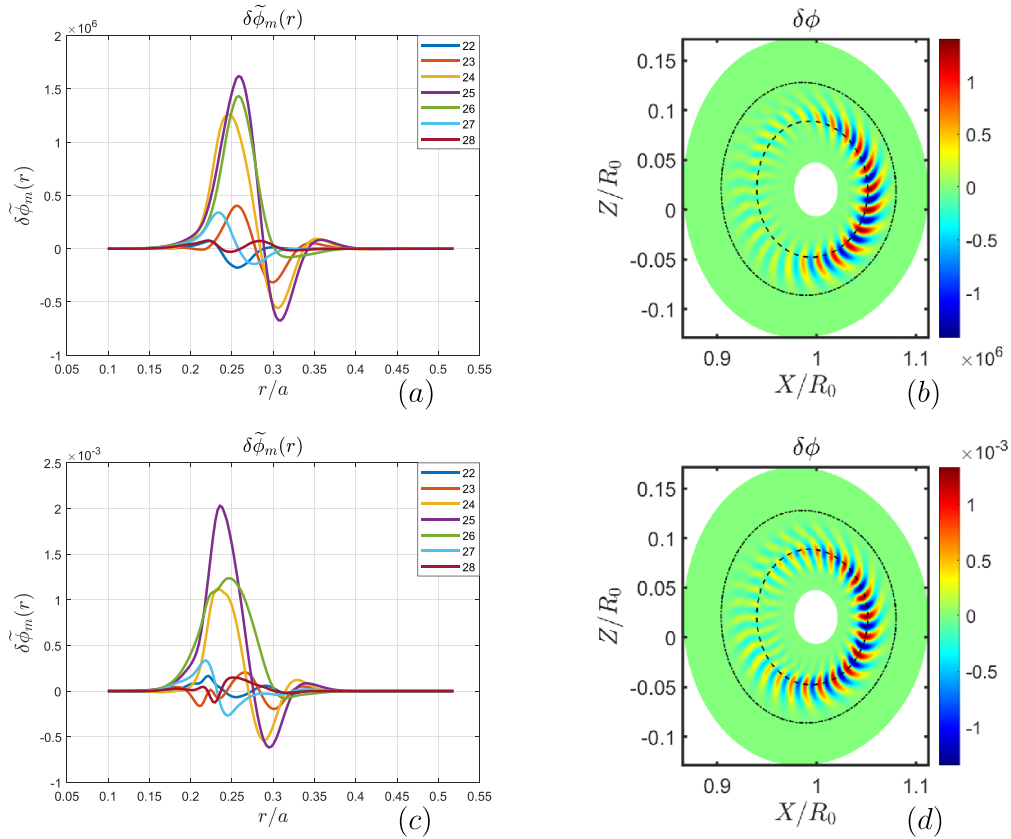


Figure 3. Radial structures of poloidal harmonics (a), (c) and poloidal mode structure of the real part of electrostatic potential (b), (d) for a toroidal eigenmode $n = 25$ from the trapped electron (a), (b) and adiabatic electron (c), (d) simulations. In figures (b), (d), the dashed line and dashed-dotted line indicate the largest η_i and q_{\min} positions, respectively.

in the maximal gradient region as shown in figures 3(a) and (c), due to the flat q profile. Clearly, there is not the scale-length separation between the mode envelope and poloidal harmonics. Furthermore, the standard balloon theory breaks down when the magnetic shear is $s \sim 0$ [37]. Therefore, the first-principles global gyrokinetic simulation approach used in this work is required to study the unique ITG mode structure in the ITB plasmas.

Note that previous gyrokinetic simulations have shown that the trapped electrons can enhance the ITG mode growth

rate by reducing the adiabatic electron shielding effect on the electrostatic potential by a factor of the trapped electron fraction in equation (12) [21]. In the concentric circular geometry and normal magnetic shear of plasmas, this effect is dominant since most trapped electrons do not resonate with the ITG mode [21]. However, in our work, the ITG growth rate from the non-adiabatic electron simulations is 2–4 times higher than that from adiabatic electron simulations, as shown in figure 2(a), which cannot be explained by the above mechanism alone because the fraction of trapped

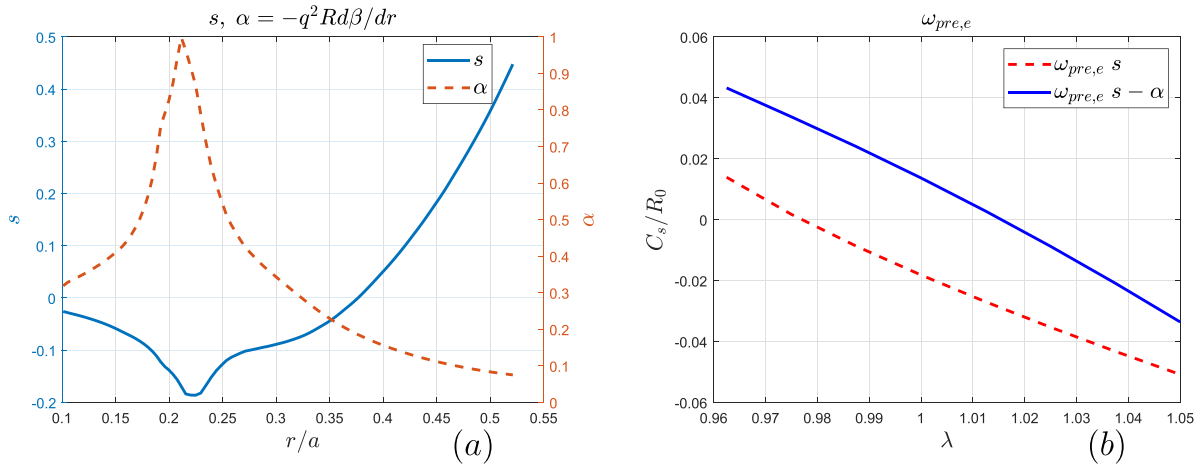


Figure 4. Radial profiles of magnetic shear $s = (rdq)/(qdr)$ and $\alpha = -q^2 R_0 d\beta/dr$ parameter (a) and precession drift frequency of trapped electrons $\omega_{pre,e}$ (b). The dashed and solid lines in (b) represent the theoretical precession frequencies without and with α effect correction, respectively, based on the s and α profiles in (a).

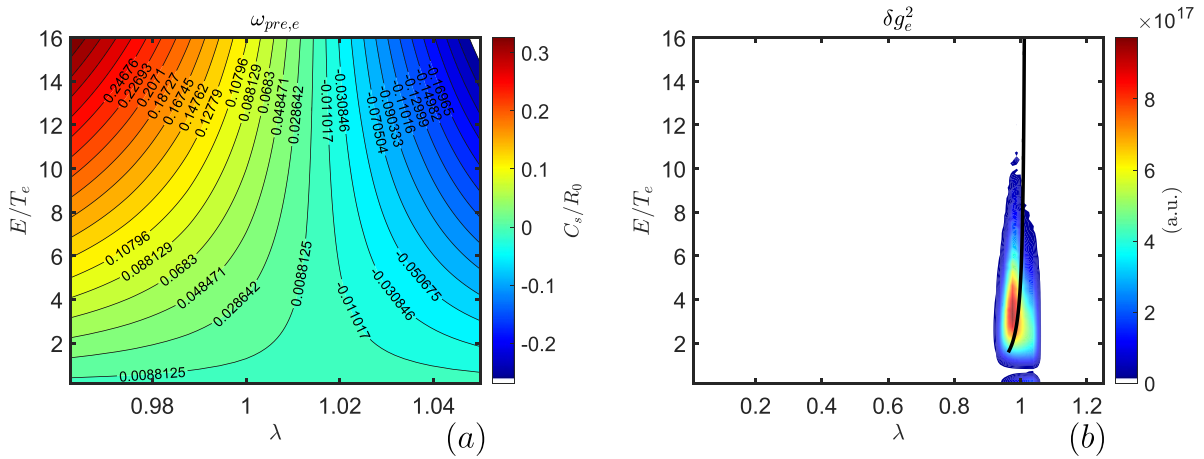


Figure 5. Under the EAST equilibrium configuration, (a) the contour plot of $\omega_{pre,e}$ in $E - \lambda$ space, and (b) phase space structures of $(\delta g_e/f_{e0})^2$, solid line is resonance for trapped electron precession frequency $\omega = n\omega_{pre}$ corresponding to ITG (the real frequency of ITG turbulence $\omega = 0.85R_0/C_s$ for toroidal eigenmode $n = 25$).

electrons is only about 20% in the ITB region. Thus, the resonance effect between the trapped electron and the ITG may become important, since the weak negative magnetic shear and large Shafranov shift would reverse the precession direction of the trapped electron [22]. It has been shown that the growth rate of TEM is greatly reduced by the effects of negative magnetic shear and large Shafranov shift [3, 17, 22, 23].

3.2. Trapped electrons resonate with ITG mode through precession drift reversal

In general, the resonance condition [38] for low-frequency waves in axisymmetric systems is $\omega - n\omega_{pre} - p\omega_b = 0$ for trapped particles, where p is an integer number, and ω_{pre} and ω_b are the precessional and bounce frequencies, respectively [39]. For typical tokamak parameters, the trapped electron bounce frequency is too high to resonate with the ITG mode, while the trapped electron precession frequency can be close to the ITG frequency, with the precession direction depending on the magnetic shear (weak or reversed is favored) and large

Shafranov shift. In EAST discharge #93890, the magnetic shear is weakly negative and the Shafranov shift (α effect) is large in the ITB region, which can be seen in figure 4(a). Correspondingly, the toroidal precession drift frequency for the pitch angle $\lambda = \mu B_0/E$ by analytical calculation [40, 41] is shown in figure 4(b). Here, E is the trapped electron kinetic energy. It is seen that the trapped electron precession drift is along the ion diamagnetic drift direction by using the s and α values at the radial location of the ITG mode.

To identify the wave-particle resonance channels, in figure 5 the contour line of the theoretical precession drift [40, 41] and the square of the perturbed distribution function of trapped electrons normalized by the background equilibrium as $(\delta g_e/f_{e0})^2$ (representing the relative strength of resonance interaction) [42] are computed in the $(E - \lambda)$ phase space. As shown in figure 5, the precession drift frequency of the trapped electrons (after multiplying the toroidal number $n = 25$) matches well with the ITG frequency, and the center of the resonant island from GTC simulation is close to the theoretical calculation, which shows the precession resonance

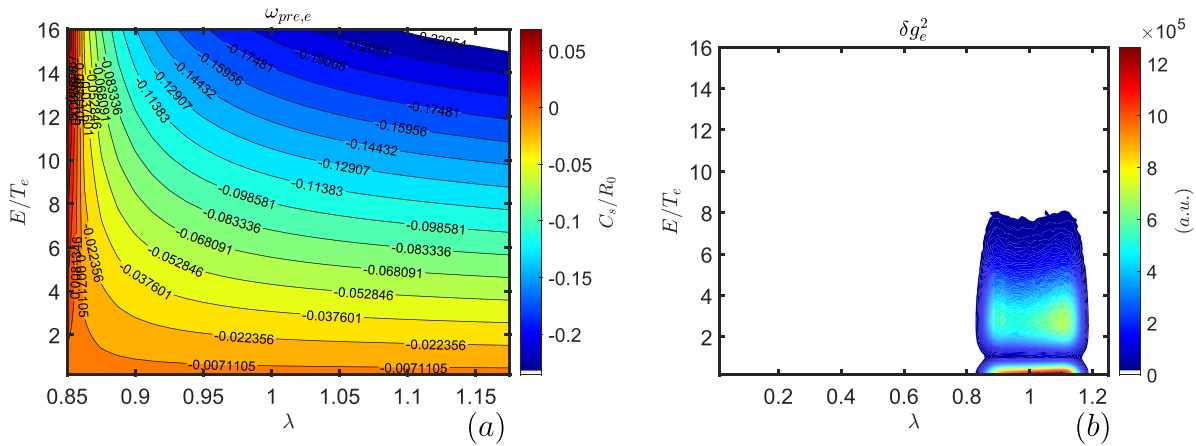


Figure 6. Under the CBC parameters, (a) the contour plot of $\omega_{pre,e}$ in $E - \lambda$ space, and (b) phase space structures of $(\delta g_e/f_{e0})^2$.

between ITG and trapped electrons in ITB plasmas. Moreover, the location and the shape of the resonant region are determined by the resonant particle amount and the dependence of the precession drift on $(E - \lambda)$. For comparison, in figure 6 we analyze δg_e^2 of trapped electrons in $(E - \lambda)$ space for the unstable ITG mode using CBC magnetic geometry in the zero-beta limit, where the large and normal magnetic shear is applied and the Shafranov shift is zero. From figure 6(b) it is seen that the amplitude of δg_e^2 in the high-energy tail peaks at zero E , which is similar to the adiabatic response that is proportional to the equilibrium Maxwellian. Thus, in contrast to the resonance mechanism of ITG destabilization by trapped electrons in the ITB case in figure 5, the non-adiabatic density of trapped electrons on the RHS of equation (12) can partially cancel with the adiabatic electron shielding term on the LHS of equation (12) as illustrated in [21]. Therefore, in the ITB region, the weakly negative magnetic shear and large Shafranov shift can reverse the precession drift direction for bulk trapped electrons and thus eliminate most drive of TEM instability. In addition, the experimental results of density fluctuation measured by the CO₂ laser collective scattering diagnostic also support the view that the TEM instability is suppressed [6]. However, the trapped electrons with precession drift reversal can strongly resonate with the ITG instability and significantly enhance the ITG growth rate, thereby driving large turbulent transport.

4. Nonlinear simulation results

4.1. Zonal flow can regulate turbulence with adiabatic electron simulations

In this section, nonlinear simulations are performed to study the saturation and transport mechanisms of ITG in the ITB region. Zonal flow, the primary saturation mechanism of ITG turbulence, generated by turbulence, plays an important role in regulating turbulence and transport [8, 10, 12, 27, 43]. It was also found that the evolution of the zonal flow was not significantly affected by the trapped electrons [19]. However, our linear simulation results show that the resonance effects between the trapped electrons and the ITG mode are dramatic

Table 1. Different nonlinear simulation cases.

Case	Description
(I)	Adiabatic electron model, turn on zonal flow (zonal component of adiabatic electron $\langle n_e \rangle = 0$ in equation (6))
(II)	Adiabatic electron model, turn off zonal flow (remove equation (6))
(III)	Trapped electron model, turn on zonal flow (self-consistently keep both $\langle n_i \rangle$ and $\langle n_e \rangle$ in equation (6))
(IV)	Trapped electron model, turn off zonal flow (remove equation (6))
(V)	Trapped electron model, turn on zonal flow (self-consistently keep $\langle n_i \rangle$ and artificially drop $\langle n_e \rangle$ in equation (6))

in the ITB region. Therefore, the non-adiabatic effect of the trapped electron may play an important role in both turbulence and zonal flow in the nonlinear stage. Thus, as shown in table 1, five separate nonlinear simulations from case (I) to case (V) are performed with different combinations of zonal flow and trapped electrons.

Both case (I) and case (II) apply adiabatic electron models, which are identical in the linear stage and different in the nonlinear stage, where the nonlinearly generated zonal flow is kept in case (I), while it is artificially removed in case (II). As shown in figure 7, the ITG turbulence saturates at a much lower amplitude with a much lower heat conductivity of ions in case (I), with self-consistent zonal flow dynamics, compared with case (II), where the zonal flow is artificially removed. In figure 7(a), the regulation mechanism between turbulent and zonal flow can be clearly seen. When the zonal flow is weak at the beginning, the turbulent flow intensity increases continuously; meanwhile, the zonal flow evolves to a certain intensity, and the turbulent flow begins to enter the saturation stage. Moreover, the radial structures and time evolutions of zonal flow and thermal ion zonal density from case (I) are shown in figure 8, where it can be seen that the correlations are consistent with equation (6). It is found that the radial scale length of the zonal flow is shorter than that of the ITG streamers in

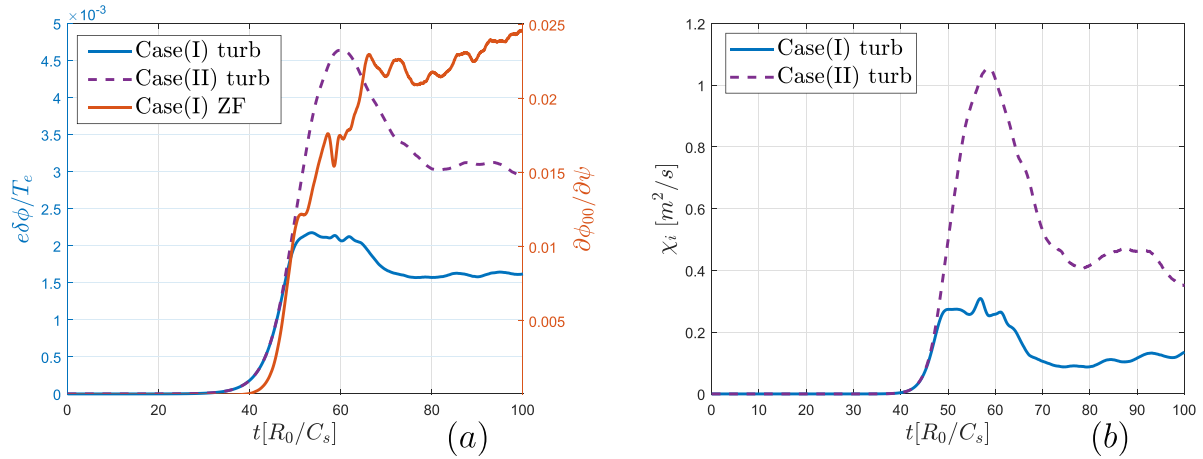


Figure 7. Time evolutions for the volume-averaged (a) turbulence ϕ and (b) thermal ion heat diffusivity from the simulations with (case (I)) and without (case (II)) self-consistently generated zonal flow.

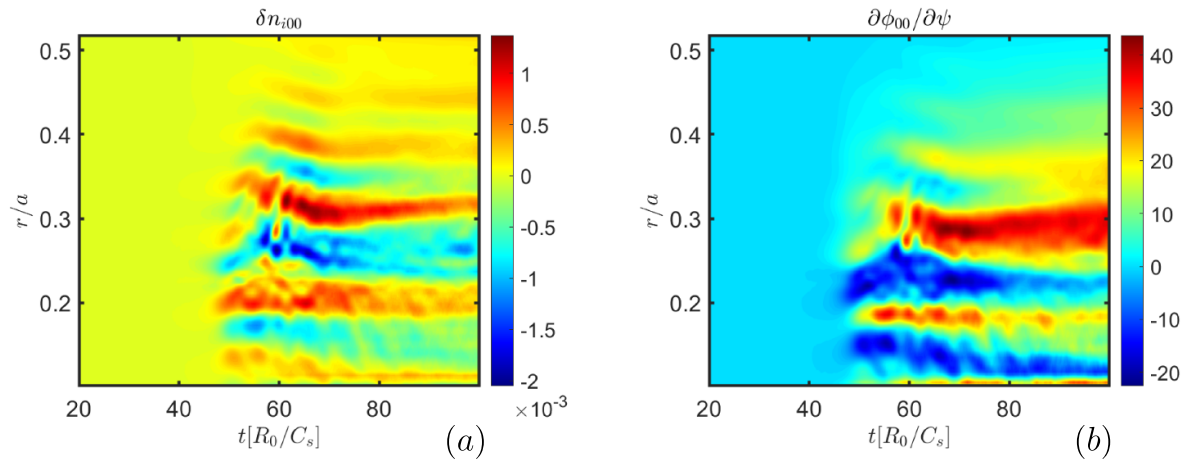


Figure 8. The time evolutions of (a) δn_{i00} and (b) $\partial\phi_{00}/\partial\psi$ radial profiles from case (I) using adiabatic electrons.

figure 8, which confirms the importance of zonal flow regulation in ITG turbulence when using the adiabatic electron model.

For nonlinear simulations with the non-adiabatic electron model, the zonal flow is self-consistently kept in case (III) and artificially removed in case (IV), similar to the above cases with the adiabatic electron model. In case (V), the zonal flow is kept and computed only considering the thermal ion zonal density, while the trapped electron zonal density is dropped in equation (6). First, as shown in figure 9, after considering the non-adiabatic effect of trapped electrons, the heat conductivity of ions and the turbulence intensity increase by at least seven times compared with those in the adiabatic electron model. Moreover, after considering the non-adiabatic effect of trapped electrons, the linear growth rate of the ITG is larger, so the instability will enter the saturation stage faster. Previous studies have found that the non-adiabatic effect of trapped electrons increases the heat conductivity of ions by a factor of 2–3 with the positive magnetic shear q profile [19–21]. Here, since the linear growth rate of ITG turbulence is drastically enhanced, the amplitude of turbulent saturation increases, and thus the ion heat transport is greatly enhanced. On the other

hand, the adiabatic electron response to the non-zonal potential does not drive the radial particle flux, and the adiabatic electron will not respond to the zonal potential [44, 45]. The non-adiabatic response of trapped electrons reduces the intensity of the zonal flow and further enhances the turbulent transport. This will be confirmed below.

Next, we compare the time evolutions of ITG turbulence and zonal flow intensities between cases (III)–(V). It is found in figure 10 that the turbulence intensities from case (III) with zonal flow and case (IV) without zonal flow are comparable with each other, which indicates that zonal flow regulation is not important when the trapped electrons are included, in contrast to the adiabatic electron results from cases (I) and (II). In figure 10, an interesting feature can be seen in that the turbulence intensity in case (V) is lower than in both cases (III) and (IV), along with a stronger zonal flow contributed only by thermal ions, which indicates that trapped electrons weaken the zonal flow and consequently enhance the ITG turbulence. The corresponding turbulent transport properties of cases (III)–(V) are shown in figure 11, where the evolutions of particle diffusivity and heat conductivity of both ion and electron species are consistent with the

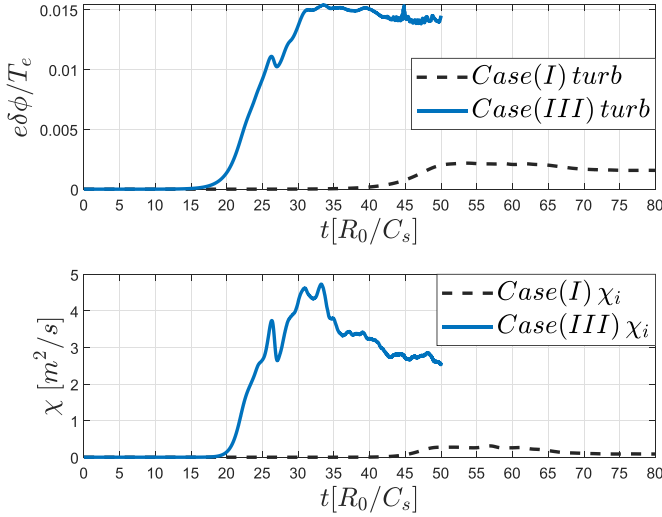


Figure 9. The time history for volume-averaged (top panel) turbulence $\delta\phi$ and (bottom panel) heat diffusivity of ions from case (I) and case (III).

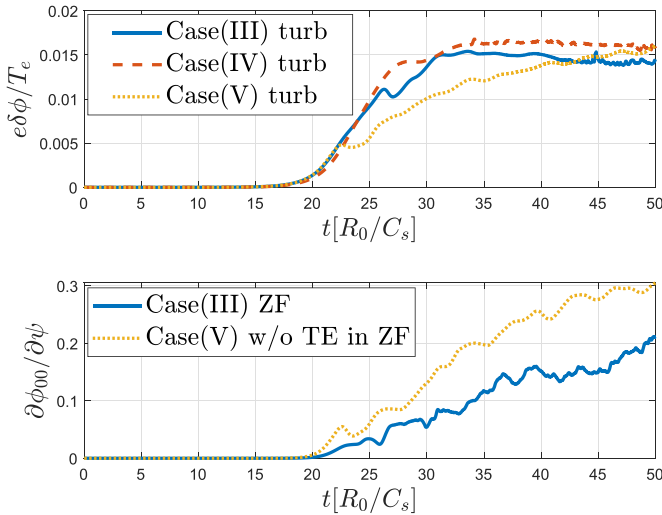


Figure 10. The time history for volume-averaged (top panel) turbulence $\delta\phi$ and (bottom panel) zonal flow $\partial\phi_{00}/\partial\psi$ from cases (III)–cases (V) using trapped electrons. Note that zonal flow is artificially removed in case (IV).

turbulence intensity in figure 10. It is similar to recent simulations of turbulent transport in the configuration of the LHD stellarator [44]. However, it is different from the results obtained under the positive magnetic shear configuration of the tokamak, where the enhancement of turbulent transport was mainly attributed to the increase in the ITG linear growth rate after considering the non-adiabatic effect of trapped electrons [19–21]. It should be noted that, with respect to each case in figure 11(a), the volume-averaged ion and electron particle diffusivity (D_i and D_e) are equal to each other due to the ambipolar particle fluxes. As shown in figure 11(b), after nonlinear saturation, the heat conductivity of electrons is generally 1.5 times larger than that of ions. Electron heat conductivity is larger because ITG is mostly driven by trapped electrons. Clearly, both the ion and electron heat conductivities shown

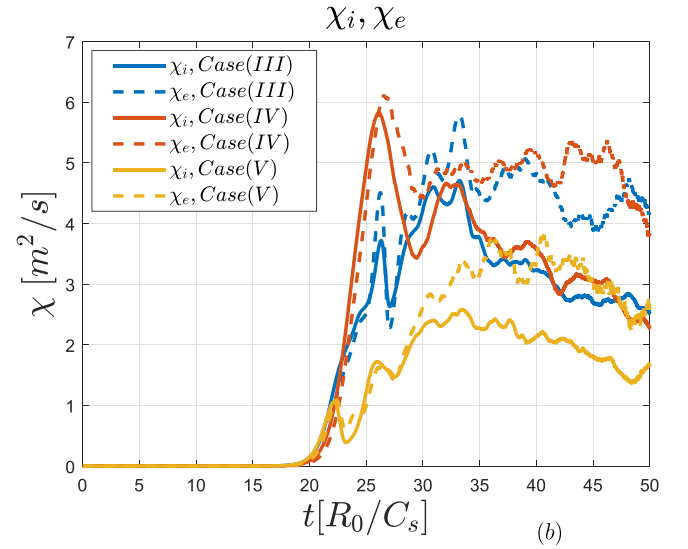
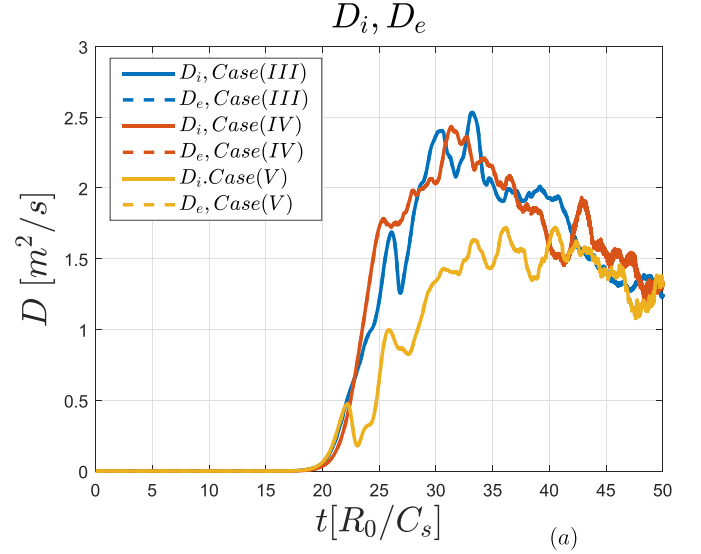


Figure 11. The time history for volume-averaged (a) particle diffusivity and (b) heat conductivity of ion and electron species from case (III)–case (V) using kinetic trapped electrons.

in figure 11(b) are larger than the results of power balance analysis by the ONETWO code (at the location of ITB, the heat conductivities of both ions and electrons are less than $1 \text{ m}^2 \text{ s}^{-1}$), as shown in figure 8 of [6]. This is because there are still many factors not considered in the current GTC simulations, such as the shear caused by the toroidal rotation and the mean flow caused by the radial electric field.

4.2. Zonal flow reduction due to the ambipolar ion and electron particle fluxes

To further illustrate how trapped electrons reduce the zonal flow, the radial structures of the time evolution of thermal ion and electron zonal densities, i.e. δn_{i00} and δn_{e00} from cases (III) and (V), are compared in figure 12. Note that although the δn_{e00} is artificially dropped in equation (6) for solving the zonal flow in case (V), it can still be calculated from the trapped electrons at each time step for comparison with case

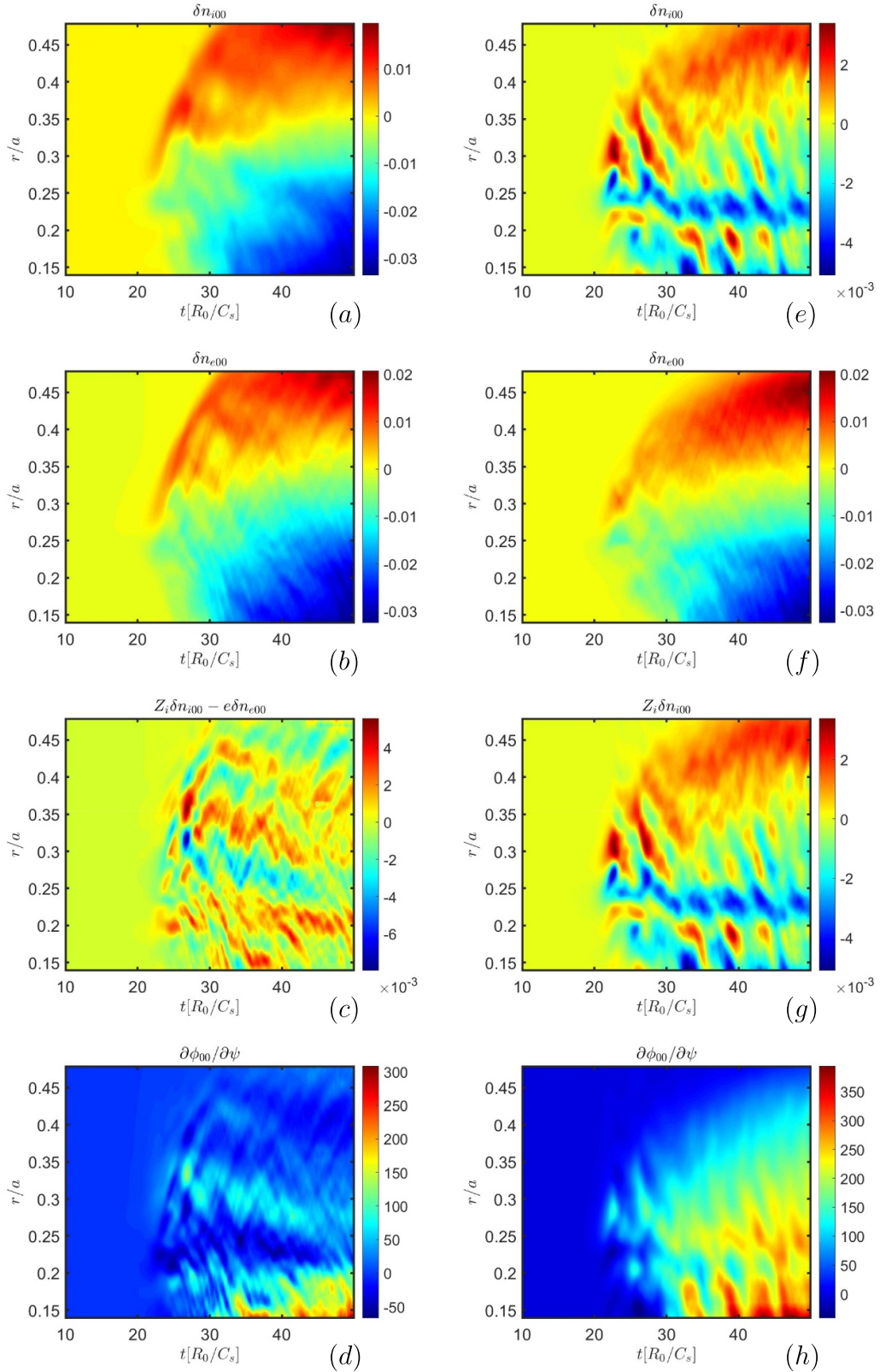


Figure 12. Comparisons of the radial-time plots of δn_{i00} , δn_{e00} , $Z_i \delta n_{i00} - e \delta n_{e00}$ and $\partial \phi_{00} / \partial \psi$ between case (III) (left column) and case (V) (right column).

(III) in figure 12(f). For case (III), the δn_{i00} exhibits a similar structure to δn_{e00} in the radial-time plots as shown in figures 12(a) and (b), where a severe cancellation between

$Z_i \delta n_{i00}$ and $-e \delta n_{e00}$ arises due to the ambipolar gyro-center particle fluxes in figure 12(c), which results in a much smaller net zonal density. In contrast, the δn_{i00} radial structure and

time evolution in case (V) are not affected by trapped electrons, because the zonal quasi-neutral condition for case (V) indicates that the sum of zonal ion polarization density and zonal ion gyro-center density is zero, while the zonal trapped electron density is not considered, and thus the gyro-center particle fluxes are non-ambipolar for the zonal components in case (V). Instead, δn_{i00} in case (V) is close to case (I) using the adiabatic electron model, but at a higher amplitude due to the stronger linear growth in the presence of kinetic trapped electrons. Moreover, δn_{e00} exhibits similar structures in figures 12(b) and (f) between cases (III) and (V), indicating its robust drive from the ITG turbulence stress. Meanwhile, as we can see in figures 12(d) and (h), the zonal flow in case (III) has a large intensity only very close to the core; however, the zonal flow in case (V) becomes significantly larger, and the radial structure range is wider. Thus, we can conclude that resonant trapped electrons have important effects on the intensity of the zonal flow as well as on the saturation and transport levels of ITG turbulence in the nonlinear stage, which significantly reduce the zonal flow generation due to the ambipolar gyro-center particle fluxes, and thus weaken the zonal flow regulation and amplify the ITG turbulent transport.

5. Conclusions

In this paper, the effects of trapped electrons on ITG turbulence are investigated by electrostatic simulations using the GTC based on the experiment in EAST with ITB plasma.

In the linear stage, under this equilibrium configuration of weakly negative magnetic shear q profile and large pressure gradient, the precession drift of the trapped electrons reverses near the core, then the resonance between the ITG and trapped electrons becomes effective. Thus, the linear growth rate and frequency of the ITG instability are enhanced dramatically by the non-adiabatic effect of the trapped electrons, which agrees well with the results obtained by NTL code [6, 46]. This resonant enhancement by the resonance between trapped electrons and ITG due to the negative magnetic shear and strong Shafranov shift is in addition to the well-known non-resonant enhancement by trapped electrons in the positive magnetic shear, where it was shown that the linear growth rate of ITG increases due to the trapped electrons reducing the adiabatic electron shielding effect on the electrostatic potential [19–21]. On the other hand, the TEM instability is suppressed mainly due to the negative magnetic shear and the Shafranov shift. This is consistent with previous studies [3, 22, 23, 26] and agrees well with the experimental results [6].

Considering the non-adiabatic effect of trapped electrons, it is shown that both the turbulence and heat conductivity of the particles significantly increase by at least a factor of 7 compared with those only including the adiabatic effect of electrons. The linear growth rate greatly increases due to the resonance between trapped electrons and the ITG mode. Consequently, the amplitude of turbulence and transport are significantly enhanced. Furthermore, the non-adiabatic effect of trapped electrons also reduces the intensity of the zonal flow due to the ambipolar gyro-center particle fluxes. That is, the

zonal charge density of trapped electrons and thermal ions cancels each other, weakening the intensity of the zonal flow, thereby reducing the zonal flow regulation of electrostatic turbulence and enhancing the particle and heat transport of turbulence. This is different from the previous simulation results obtained under positive magnetic shear plasmas, where the enhancement of turbulent transport was mainly attributed to the increase in the ITG linear growth rate after considering the non-adiabatic effect of trapped electrons [19–21].

It is pointed out that the transport obtained in the simulation is larger than that expected inside the ITB, since some effects such as the effect of the equilibrium shear flow and electromagnetic effect are not included. These will be studied in the future.

Data availability statement

The data that support the findings of this study are available from the corresponding author upon reasonable request.

Acknowledgments

The authors acknowledge useful discussions with P. L. Liu, X. S. Wei, B. L. Hao and X. Chen. This work was supported by the National Natural Science Foundation of China (Grant Nos. 11822505, 11905290, 11835016 and 12025508), the China National Magnetic Confinement Fusion Science Program (Grant No. 2018YFE0304100), the Youth Innovation Promotion Association CAS, the Users with Excellence Program of Hefei Science Center CAS (Grant Nos. 2019HSC-UE013 and 2021HSC-UE018), the Science Foundation of the Institute of Plasma Physics, Chinese Academy of Sciences (No. DSJJ-2021-04), the Fundamental Research Funds for the Central Universities (Grant No. WK3420000008), the Collaborative Innovation Program of Hefei Science Center CAS (Grant No. 2019HSC-CIP014), and US DOE SciDAC ISEP. This research used the resources of the Hefei advanced computing center and the National Supercomputer Center in Tianjin.

ORCID iDs

Bin Zhang  <https://orcid.org/0000-0003-0304-2372>

Wenlu Zhang  <https://orcid.org/0000-0002-7136-2119>

Huishan Cai  <https://orcid.org/0000-0002-2500-3721>

References

- [1] Wootton A.J., Carreras B.A., Matsumoto H., McGuire K., Peebles W.A., Ritz C.P., Terry P.W. and Zweben S.J. 1990 Fluctuations and anomalous transport in tokamaks *Phys. Fluids B* **2** 2879–903
- [2] Koide Y. et al 1994 Internal transport barrier on $q=3$ surface and poloidal plasma spin up in JT-60U high- β_p discharges *Phys. Rev. Lett.* **72** 3662
- [3] Connor J.W. et al 2004 A review of internal transport barrier physics for steady-state operation of tokamaks *Nucl. Fusion* **44** R1

- [4] Ida K. and Fujita T. 2018 Internal transport barrier in tokamak and helical plasmas *Plasma Phys. Control. Fusion* **60** 033001
- [5] Gao X. *et al* 2020 Experimental progress of hybrid operational scenario on EAST tokamak *Nucl. Fusion* **60** 102001
- [6] Zhang B. *et al* 2022 Progress on physics understanding of improved confinement with fishbone instability at low q $95 < 3.5$ operation regime in EAST *Nucl. Fusion* **62** 126064
- [7] Biglari H., Diamond P.H. and Terry P.W. 1990 Influence of sheared poloidal rotation on edge turbulence *Phys. Fluids B* **2** 1–4
- [8] Diamond P.H. and Kim Y.-B. 1991 Theory of mean poloidal flow generation by turbulence *Phys. Fluids B* **3** 1626–33
- [9] Terry P.W. 2000 Suppression of turbulence and transport by sheared flow *Rev. Mod. Phys.* **72** 109
- [10] Chen L., Lin Z. and White R. 2000 Excitation of zonal flow by drift waves in toroidal plasmas *Phys. Plasmas* **7** 3129–32
- [11] Kim E.J. and Diamond P.H. 2003 Zonal flows and transient dynamics of the I-h transition *Phys. Rev. Lett.* **90** 185006
- [12] Chen L., White R.B. and Zonca F. 2004 Zonal-flow dynamics and size scaling of anomalous transport *Phys. Rev. Lett.* **92** 075004
- [13] Kessel C., Jf Manickam G.R. and Tang W.M. 1994 Improved plasma performance in tokamaks with negative magnetic shear *Phys. Rev. Lett.* **72** 1212
- [14] Mazzucato E. *et al* 1996 Turbulent fluctuations in TFTR configurations with reversed magnetic shear *Phys. Rev. Lett.* **77** 3145
- [15] Strait E.J. *et al* 1995 Enhanced confinement and stability in DIII-D discharges with reversed magnetic shear *Phys. Rev. Lett.* **75** 4421
- [16] Wolf R.C. 2002 Internal transport barriers in tokamak plasmas *Plasma Phys. Control. Fusion* **45** R1
- [17] Bourdelle C., Hoang G.T., Litaudon X., Roach C.M. and Tala T. 2005 Impact of the α parameter on the microstability of internal transport barriers *Nucl. Fusion* **45** 110
- [18] Sydora R.D., Decyk V.K. and Dawson J.M. 1996 Fluctuation-induced heat transport results from a large global 3d toroidal particle simulation model *Plasma Phys. Control. Fusion* **38** A281
- [19] Chen Y., Parker S.E., Cohen B.I., Dimits A.M., Nevins W.M., Shumaker D., Decyk V.K. and Leboeuf J.N. 2003 Simulations of turbulent transport with kinetic electrons and electromagnetic effects *Nucl. Fusion* **43** 1121
- [20] Lewandowski J.L.V., Rewoldt G., Ethier S., Lee W.W. and Lin Z. 2006 Global particle-in-cell simulations of microturbulence with kinetic electrons *Phys. Plasmas* **13** 072306
- [21] Lin Z., Nishimura Y., Xiao Y., Holod I., Zhang W.L. and Chen L. 2007 Global gyrokinetic particle simulations with kinetic electrons *Plasma Phys. Control. Fusion* **49** B163
- [22] Beer M.A., Hammett G.W., Rewoldt G., Synakowski E.J., Zarnstorff M.C. and Dorland W. 1997 Gyrofluid simulations of turbulence suppression in reversed-shear experiments on the tokamak fusion test reactor *Phys. Plasmas* **4** 1792–9
- [23] Deng W. and Lin Z. 2009 Properties of microturbulence in toroidal plasmas with reversed magnetic shear *Phys. Plasmas* **16** 102503
- [24] Dong J.Q., Mahajan S.M. and Horton W. 1997 Coupling of η and trapped electron modes in plasmas with negative magnetic shear *Phys. Plasmas* **4** 755–61
- [25] Liu S.F., Guo S.C., Kong W. and Dong J.Q. 2014 Trapped electron effects on η -mode and trapped electron mode in RFP plasmas *Nucl. Fusion* **54** 043006
- [26] Dimits A.M. *et al* 2000 Comparisons and physics basis of tokamak transport models and turbulence simulations *Phys. Plasmas* **7** 969–83
- [27] Lin Z., Taik Soo Hahm W.W.L., Tang W.M. and White R.B. 1998 Turbulent transport reduction by zonal flows: massively parallel simulations *Science* **281** 1835–7
- [28] Hahm T.S. 1988 Nonlinear gyrokinetic equations for tokamak microturbulence *Phys. Fluids* **31** 2670–3
- [29] Brizard A.J. and Hahm T.S. 2007 Foundations of nonlinear gyrokinetic theory *Rev. Mod. Phys.* **79** 421–68
- [30] Lin Z., Tang W.M. and Lee W.W. 1995 Gyrokinetic particle simulation of neoclassical transport *Phys. Plasmas* **2** 2975–88
- [31] Lin Z., Hahm T.S., Lee W.W., Tang W.M. and Diamond P.H. 1999 Effects of collisional zonal flow damping on turbulent transport *Phys. Rev. Lett.* **83** 3645–8
- [32] Holod I., Zhang W.L., Xiao Y. and Lin Z. 2009 Electromagnetic formulation of global gyrokinetic particle simulation in toroidal geometry *Phys. Plasmas* **16** 122307
- [33] Xiao Y., Holod I., Wang Z., Lin Z. and Zhang T. 2015 Gyrokinetic particle simulation of microturbulence for general magnetic geometry and experimental profiles *Phys. Plasmas* **22** 022516
- [34] Parker S.E. and Lee W.W. 1993 A fully nonlinear characteristic method for gyrokinetic simulation *Phys. Fluids B* **5** 77–86
- [35] Dimits A.M. and Lee W.W. 1993 Partially linearized algorithms in gyrokinetic particle simulation *J. Comput. Phys.* **107** 309–23
- [36] Lin Z. and Chen L. 2001 A fluid–kinetic hybrid electron model for electromagnetic simulations *Phys. Plasmas* **8** 1447–50
- [37] Connor J.W., Hastie R.J. and Taylor J.B. 2004 Stability of toroidal plasmas: the influence of magnetic shear, periodicity and rotation *Plasma Phys. Control. Fusion* **46** B1
- [38] Chen L. 1999 Theory of plasma transport induced by low-frequency hydromagnetic waves *J. Geophys. Res.: Space Phys.* **104** 2421–7
- [39] White R.B. 2013 *Theory Of Toroidally Confined Plasmas* (London: Imperial College Press)
- [40] Graves J.P. 2013 Toroidal drift precession and wave–particle interaction in shaped tokamaks with finite beta and neoclassical equilibrium effects *Plasma Phys. Control. Fusion* **55** 074009
- [41] Connor J.W., Hastie R.J. and Martin T.J. 1983 Effect of pressure gradients on the bounce-averaged particle drifts in a tokamak *Nucl. Fusion* **23** 1702
- [42] Zhang H.S. and Lin Z. 2010 Trapped electron damping of geodesic acoustic mode *Phys. Plasmas* **17** 072502
- [43] Diamond P.H., Itoh S.I., Itoh K. and Hahm T.S. 2005 Zonal flows in plasma a review *Plasma Phys. Control. Fusion* **47** R35
- [44] Singh T., Nicolau J.H., Lin Z., Sharma S., Sen A. and Kuley A. 2022 Global gyrokinetic simulations of electrostatic microturbulent transport using kinetic electrons in LHD stellarator *Nucl. Fusion* **62** 126006
- [45] Garbet X., Idomura Y., Villard L. and Watanabe T.H. 2010 Gyrokinetic simulations of turbulent transport *Nucl. Fusion* **50** 043002
- [46] Lei Y., Yingfeng X., Xiao X., Dai Z. and Wang S. 2016 A gyrokinetic continuum code based on the numerical Lie transform (NLT) method *J. Comput. Phys.* **316** 180–92